RSC Advances

Solvothermal Synthesis of 1D Nanostructured Mn_2O_3: Effect of Ni^{2+} and Co^{2+} Substitution on the Catalytic Activity of Nanowires

Xiaoran Niu [a], Huiying Wei [a], Ke Tang[a], Wei Liu [a], Genyuan Zhao [a], and Yanzhao Yang* [a]

a Key Laboratory for Special Functional Aggregate Materials of Education Ministry, School of Chemistry and Chemical Engineering, Shandong University, Jinan, 250100, P. R. China. Fax: +86-531-88564464; Tel: +86-531-88362988; E-mail: yzhyang@sdu.edu.cn.

In this paper, cations modified one dimensional Mn_2O_3 nanowires were synthesized via a solvothermal synthesis and calcinations free from the template-assisted methods. The samples were characterized in detail by transmission electron microscopy (TEM), scanning electron microscopy (SEM), X-ray diffraction (XRD), Raman spectroscopy, high resolution transmission electron microscopy (HRTEM), X-ray photoelectron spectroscopy (XPS). XRD results revealed the homogeneity of Ni-Mn-O/Co-Mn-O solid solutions. By introducing the two different cations the Mn_2O_3 nanowires can be freely manipulated. The H_2-TPR measurement showed the enhanced reduction behaviors of the doped Manganese oxide (Mn_2O_3) samples. The presence of Ni^{2+} and Co^{2+} produced lattice defects and promoted the production of oxygen vacancies, which explained the results that Ni^{2+}/Co^{2+} doped Mn_2O_3 showed higher catalytic activity than the pure one.

1 Introduction

For decades, nanostructural materials have become one of the hottest topics in the field of materials science, among which one-dimensional (1D) metal-oxide nanostructures have attracted special attention because metal oxides are the most fascinating functional materials.[1-4] The 1D morphologies can easily enhance the practical applications of the metal-oxide nanostructures, including gas sensors[5-7], supercapacitors[8,9], nanocatalysts[10-13], and biosensors[14,15]. Additionally, low-dimensional nano-structured materials make it possible to improve their functionalities through an increase in the surface area and quantum confinement effects.[2] manganese oxides (Mn_2O_3), as one of the most important transition oxides, is commonly used as the oxide support in the three-way catalyst. Generally, the catalytic activity of Mn_2O_3 originates from the terminated surface oxygen and affected by large specific surface area. Thus, an increase in the specific surface area and in concentration of active oxygen located at the Mn_2O_3 surface is favorable methods to promote catalytic activity. Notably, the active oxygen located at the Mn_2O_3 surface is relative to reactive facets, surface defects (oxygen vacancies) and surface element composition.[16-18] As is known, the shape-selective synthesis of Mn_2O_3 nanostructures is demonstrated to be a powerful method to promote their catalytic performance. For example, Zhang et al. reported flower-liked Mn_2O_3 dominated by (211) and (200) planes, selectively prepared by a facile hydrothermal method, showed an enhanced catalytic activity towards CO oxidation compared with Mn_2O_3 nanocubes.[19]

It is well known that cation substitution can provide an effective tool for tailoring the physicochemical properties of metal oxides[20,21], in which case the functionalities of Mn_2O_3 nanomaterials can be optimized by goal-directed control of the cation composition. So far, there are only a few reports about the method by changing surface element composition to promote the active oxygen content at the Mn_2O_3 surface, which will ultimately reveals strikingly high catalytic activity. For one instance, Ca^{2+} ion doped manganese oxides ($CaMn_2O_4$, $CaMnO_3$ and $Ca_2Mn_2O_8$) have been reported to enhance the catalytic activity of manganese oxides for water oxidation.[22-24] Indeed, the homogeneously Ni doped CeO_2 nanostructures displayed excellent catalytic activity towards CO oxidation.[25] Copper doped ceria nanospheres exhibit higher catalytic activity than pure CeO_2 nanospheres.[26] We have previously shown that doping of carbonate with cobalt ions can produce enhanced catalytic performance towards CO oxidation.[27] Generally, Surface oxygen vacancies promote high dispersion and strong anchoring of transition metal ions on the metal oxides surface. Compared with the three-dimensional (3D) nanostructure, the high aspect ratio of 1D nanowires expose the surface oxygen vacancies on the surface of the nanostructure rather than embedding them in the bulk.[28]

Thus, in this work, we for the fist time present the fabrication of Ni^{2+} and Co^{2+} ions-substituted manganese oxide nanowires via the template-free solvothermal synthesis. The samples were characterized by TEM, HRTEM, XRD, Raman spectroscopy and XPS. The preliminary catalytic studies revealed that the Ni^{2+}, Co^{2+} ions-doped Mn_2O_3 nanowires had strikingly higher catalytic activity than pure Mn_2O_3 nanowires and commercial Mn_2O_3.

2 Experimental

2.1 Materials

All the chemical reagents were of analytical grade, purchased from Sinopharm Chemical Reagent Co. Ltd (China) and used as received without further purification.

2.2 The synthesis of Ni^{2+}-and Co^{2+}- doped Mn_2O_3 nanowires

0.1 g of PVP (K30) and 0.06 g ethylenediaminetetraacetic acid disodium salt (EDTA disodium salt) were dissolved into the mixture solution of 5 mL H_2O and 1 mL of N, N-dimenthyl-formamide (DMF), $Ni(Ac)_2\cdot 4H_2O$ and $Co(Ac)_2\cdot 4H_2O$ weighed in molar ratios (M/(M + Mn)) of 5% were separately added to the above two mixture solution. After stirring for 30 min, 180 μL of $Mn(NO_3)_2$ solution (50 wt%) was added to the homogeneous solution. After stirring for another 20 min, the two mixture were transferred to two 25 mL Teflon-lined stainless steel autoclaves, respectively. All were maintained for 21 h at 180 °C. When the autoclave was cooled at room temperature, the products were collected and washed with absolute alcohol four times sequentially. Finally, the products were dried and were further annealed at 400 °C for 12 h in air with a temperate rate of 2 °C min^{-1}. The pure without Ni^{2+} or Co^{2+}-doped Mn_2O_3 nanowires were also produced via the same procedure to make as a comparison.

2.3 Physical characterization

The crystal structure information of the synthesized samples was established by powder X-ray diffraction (XRD Bruker D8 diffractometer with Cu-Ka radiation (λ= 0.15418 nm)). The microstructure morphology of the powders was observed by using a transmission electron microscope (TEM, JEM 1011-CXII, 100KV). The field-emission scanning electron microscope (FE-SEM, Hitachi, S4800) equipped with energy-dispersive X-ray spectroscopy (EDS) and a high-resolution transmission electron microscope (HRTEM, JEM-2100, 200 kV) was used to characterize the specific morphologies. X-ray photoelectron spectroscopy (XPS) data were acquired on an ESCALAB 250 X-ray photoelectron spectrometer with Al Kα radiation and the binding energies were determined utilizing the C1s spectrum as reference at 284.7 eV. The surface areas were calculated by the Brunauer-Emmett-Teller (BET) method. Raman data were obtained using a Lab RAM HR4800 spectrometer while using a 632 nm laser line as an excitation source. The Co^{2+}, Ni^{2+} doping molar ratio in the samples were detected by an inductively coupled plasma spectrometer (ICP-AES) on an IRIS Intrepid II XSP instrument (Thermo Electron Corporation).

2.4 Temperature programmed reduction (TPR)

TPR experiments under a H_2 environment were performed on a PCA-1200 instrument. Typically, 50 mg Mn_2O_3 catalyst was pretreated under a 5% He-Ar stream at 300 ^oC for 0.5 h (heating rate = 5 ^oC min^{-1}). After cooling down to room temperature, a fow of 5% H_2-Ar was introduced into the Mn_2O_3 sample with a flow rate of 30 mL min^{-1} and the temperature was raised to 800 ^oC at a rate of 10 ^oC min^{-1}.

2.5 Catalytic experiments

The catalytic activity of the as-obtained samples was evaluated on a continuous flow fixed-bed micro-reactor operating under atmospheric pressure. In a typical experiment, 25 mg catalyst particles with 250 mg quartz sand were placed into a stainless steel tube reactor. The composition of the raw material gas is $CO/O_2/N_2$ (1 : 10 : 89). The flow rate is 60 mL·min^{-1}. The temperature of the reactor was monitored by the thermocouple placed on the catalysts, and the heating rate was 1.7 K·min^{-1}. The products from the outlet of the reactor were analyzed using an online gas chromatograph (Gasboard-3121, China Wuhan Cubic Co).

3 Results and discussions

3.1 Characteristics of nanowires

In general, crystal growth at the nanoscale is an intricate process, affected by additives such as surfactant, inorganic ions.[29] Furthermore, the crystal lattice will contract when large-sized impurities are doped to substitute the host ions (small-sized) for hetero-valence ion doping into the host lattice.[30] Here, when the reaction was carried out in the absence of Ni^{2+}, Co^{2+}(with larger radii), nanowire samples can be obtained. Fig. 1 shows TEM and SEM of as-prepared nanowire samples. On the whole,

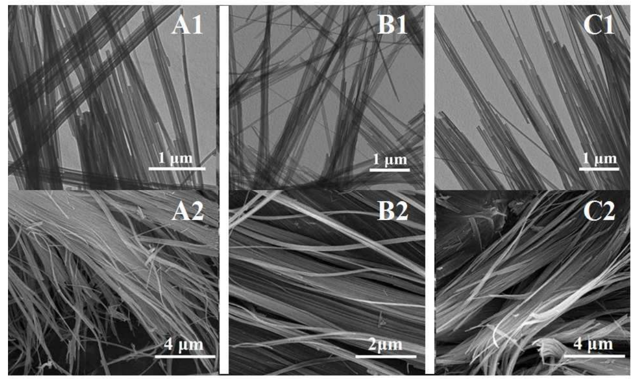

Fig. 1 TEM and SEM of the precursors of pure (A1,2) and Ni doped (B1,2) Co-doped (C1,2) Mn_2O_3.

the as-obtained nanowires were in queues length distribution. Observed in the TEM and corresponding SEM images, pure precursors (Fig.1 A1,2) have smooth surfaces with its length tens of micrometers. The Ni-doped precursors (Fig.1 B1,2) and Co-doped precursors (Fig.1 C1,2) remained the nanowire-shape well. However, the amorphous precursors were further exposed to the surroundings of 400 ^oC for 12 h to obtain the final manganese oxides.

It should be noted that the 1D nanostructure in all samples were quite thermally stable without structural collapse. Fig. 2 displays the panoramic views of the as-prepared manganese oxides. The pure sample keeps integral alignment structure with its mean diameter below 90 nm shown in Fig. 2a and the inserted magnified image. Amazingly, the Ni-doped Mn_2O_3 exposes its linearized surface with nanocrystallites (Fig. 2b) A magnified image (inserted in Fig. 2b) reveals that the well-defined Ni-doped Mn_2O_3 nanowires are constructed of nanocrystallites with a width of 50 nm, making up the diameters smaller than that of pure manganese oxides. Similarly, Fig. 2c indicates the Co-doped

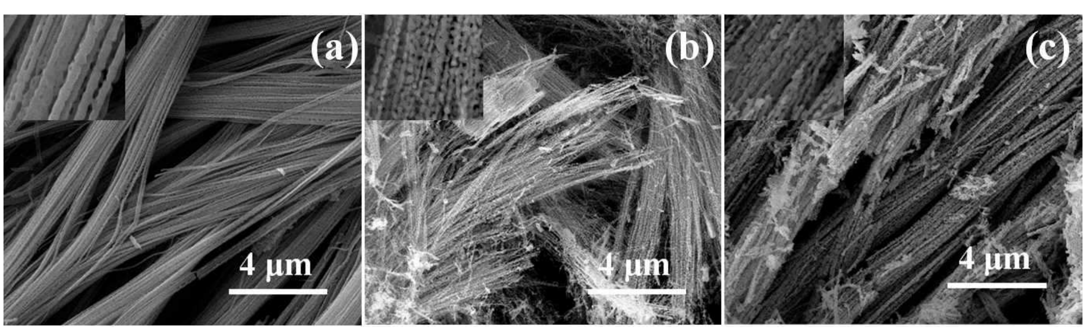

Fig. 2 SEM of the obtained Mn_2O_3: pure (a), Ni-doped (b), Co-doped (c) Mn_2O_3.The magnified images inserted on the left top.

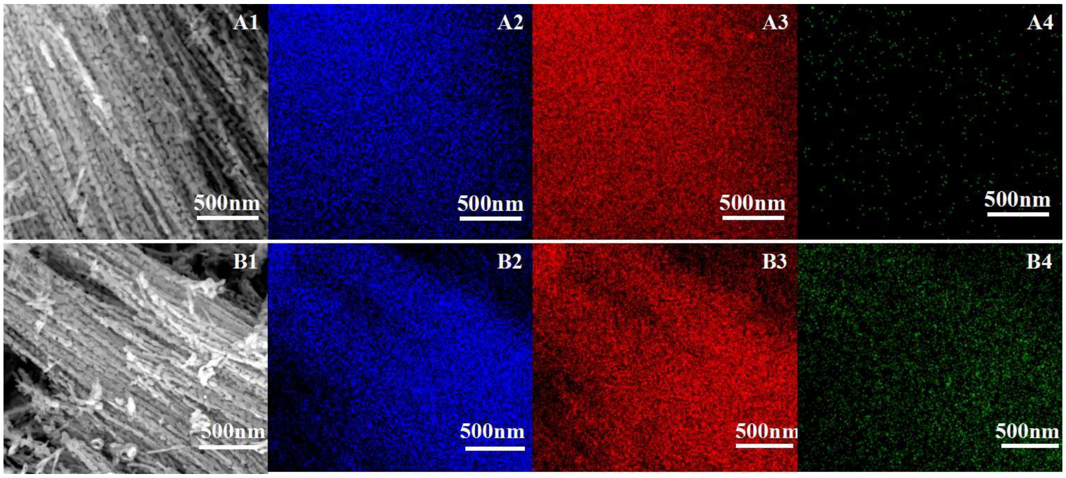

Fig.3 A1 SEM image of the Ni-doped Mn_2O_3 nanowires and (A2)–(A4) the corresponding EDS mapping patterns: Mn (blue), O (red), and Ni (green). B1 SEM image of the Co-doped Mn_2O_3 nanowires and (B2)–(B4) the corresponding EDS mapping patterns: Mn (blue), O (red), and Co (green).

Mn_2O_3 nanowires consist of nano-crystallites to keep its whole nanostructures; also, the nanowires decrease its diameter to 75 nm. The decreased diameters of the Mn_2O_3 nanowires reveal that the cobalt and nickel ions have played a pivotal role during the growth process of the Mn_2O_3. In fact, both Co^{2+} (0.072 nm) and Ni^{2+} (0.069 nm) ions can accelerate the crystal nucleation rate [27], leading shorter time for maturity, resulting in the decreased size. Inductively coupled plasma (ICP) analysis indicated that the molar ratio of doping ions in Mn_2O_3 nanostructures are 1.34% for Ni-doped Mn_2O_3 , which is lower than theoretical doping and 4.95% for Co-doped Mn_2O_3, which is close to the initial reactant composition (Table 1 in supporting). Furthermore, the corresponding EDS mapping provides a direct elemental distribution in nanowire structure. As shown in Fig. 3, Mn, O, and Ni and Mn, O, Co are uniformly distributed in the Ni-doped and Co-doped Mn_2O_3 nanowires, which confirm the homogeneity of these manganese oxide nanowires.

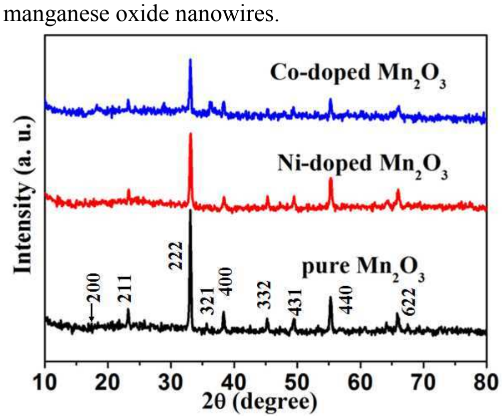

Fig. 4 XRD patterns of the synthesized pure Mn_2O_3, Ni-doped Mn_2O_3 and Co-doped Mn_2O_3

The crystal structure of the products was examined by powder X-ray diffraction (XRD). All of the samples, Mn_2O_3, Ni-doped Mn_2O_3 and Co-doped Mn_2O_3 display several peaks, corresponding to Mn_2O_3 (211), (222), (400) and (440) planes, indicating bixbyite crystal phase α-Mn_2O_3 (JCPDS no. 41-1442) (Fig. 4). It was noticed that no other peaks stemming from manganese carbonate, cobalt oxides or nickel oxides could be found, which confirm the formation of homogeneous oxide solid solutions for both samples (Ni-doped and Co-doped Mn_2O_3). In addition, a clear decrease in the peak intensity was observed in the nickel and cobalt doped samples compared to the pure Mn_2O_3, because of that doping resulted in the decrease of the degree of crystallization.

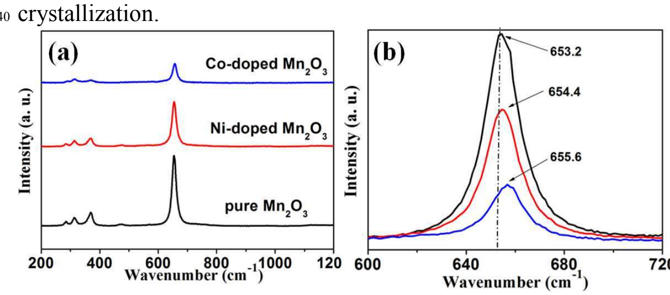

Fig. 5 Raman spectra of as-obtained Mn_2O_3, Ni-doped Mn_2O_3 and Co-doped Mn_2O_3 (a), and the magnified pattern from 600 to 720 cm^{-1} (b).

Raman scattering is an effective tool for measuring and comprehending the catalytic activity of manganese oxides and for investigating the presence of defects (such as oxygen vacancies) among doped nanomaterials.[31] The contrastive Raman spectra of pure, Ni- and Co- doped Mn_2O_3 are displayed in Fig. 5a. For pure one, three main bands at ~312, ~368,~653 cm^{-1} can be attributed to the out-of-plane bending modes of Mn_2O_3, asymmetric stretching of bridge oxygen species (Mn-O-Mn), and symmetric stretching of Mn_2O_3 groups, respectively.[32,33] The absence of the Ni-O/ Co-O characteristic peak (550/680 cm^{-1}) is indicative of the formation of solid solutions as indicated by the XRD results.[34,35] For doped Mn_2O_3, the incorporation of Co^{2+}/Ni^{2+} leads to blue shifts of the lattice Raman vibrational peak positions (Fig. 5b), confirming local structure distortion.[30,36,37] In addition, the intensity reduction and the broadening of the main Raman peak are observed, demonstrating the lattice defects occur when heterovalent Ni/Co ions are introduced as well.[37] These defects are correlated with oxygen vacancy creation for charge compensation when Mn^{3+} ions are replaced with divalent cations.

As a result, these will favor oxygen mobility and enhance the catalytic behavior of the as-prepared material. [38,39,40]

The elementary composition and chemical valence on the surface of the as-prepared nanowires were detected by X-ray photoelectron spectra (XPS). Fig. 6 shows the XPS spectrum of pure Ni-doped and Co-doped Mn_2O_3 samples. The typical binding energy (BE) peaks (such as those at 641.8 and 653.6 eV) of the Mn 2p spetrum (Fig. 6b) are observed in the as-obtained samples, which suggest the existence of Mn(III) in our products.[40] The core level peak of Co 2p (Fig. 6d blue line) at 781.8 eV is powerful to determine that the valence of Co is 2+.[41, 42] The Ni 2p spetrum (Fig. 6d red line) depicts the weak peaks due to the low Ni concentration which is verified by the above ICP ananlysis, but (BE) peaks at 855.2 can be applied to predicate that the valence state of Ni is **+2.**[43] In the O 1s XPS spectrum (Fig. 6c), the BE peak located at 529.9 eV can be indexed to the lattice oxygen of Mn_2O_3.[44] It is obvious that the shoulder width of the main BE peak is much broader than that in the pure Mn_2O_3 (black line), corresponding to the appearance of defective oxygen regions or adsorbed oxygen, indicating a better capacity for oxygen storage, which is also related to the activity of oxidization reaction. [37, 45,46]

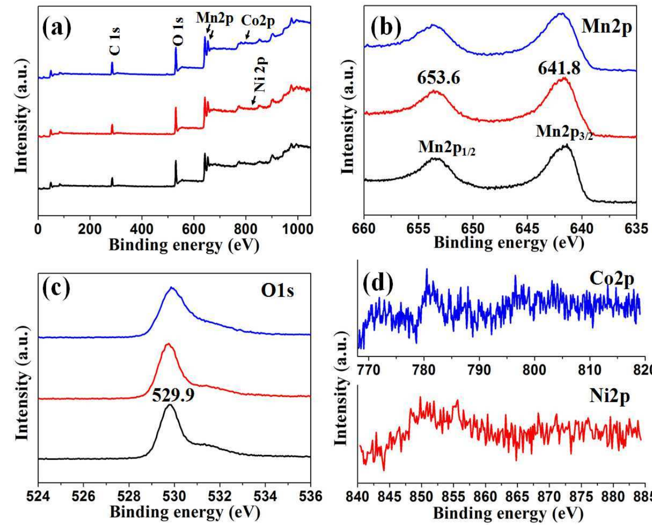

Fig.6 (a) The corresponding XPS survey spectrum of nano-wires: pure Mn_2O_3 (black line), Ni-doped Mn_2O_3 (red line) and Co-doped Mn_2O_3 (blue line); (b) Mn 2p; (c) O 1s, and (d) Co 2p and Ni 2p. (a), (b) and (c) are pure, Ni-doped and Co-doped Mn_2O_3 curves, respectively.

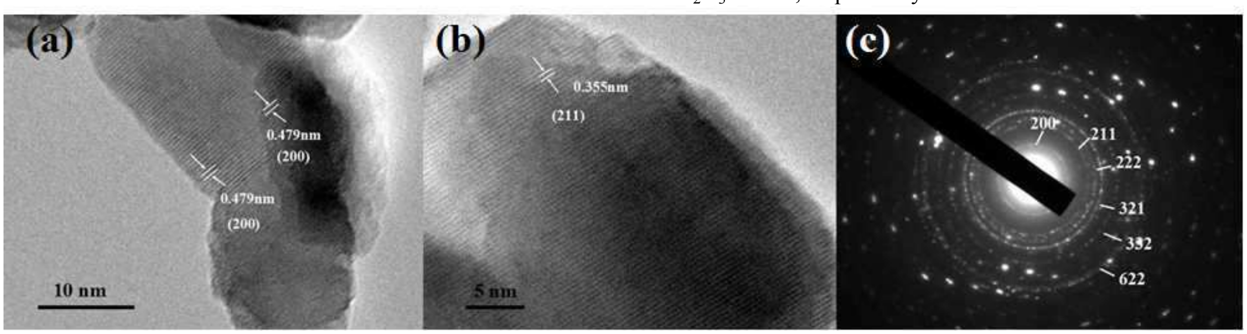

Fig.7 HR-TEM images (a) and (b), the corresponding SAED pattern (c) of the as-prepared 5 mol% Co-doped Mn_2O_3

High-resolution TEM (HRTEM) imaging was applied to investigate the detailed structure of the co-doped Mn_2O_3, which is shown in Fig. 7. Clear lattice fringes were detected in the images of Fig. 7a, and b. An interplanar spacing of about 0.479 nm corresponded to the (200) planes of Mn_2O_3, and another at about 0.355 nm was attributed to the (211) planes. Moreover, the selected-area electron diffraction (SAED) pattern (Fig. 7c) showed the characteristic diffraction rings, which were assigned to the (200), (211), (222), (321), (332) and (622) crystal planes. Indeed, the SAED pattern exhibits a set of regular spots, which demonstrate the products are formed of many small nanoparticles. Interestingly, the nanoparticles are closely packed and oriented in the same way, as confirmed by a set of electron diffraction spots in the SAED pattern. In addition, the lattice fringes with ad-spacing of 0.479 nm (see the HRTEM image in Fig. 7a) from different nanoparticles are parallel to each other.

3.2 TPR

H_2-TPR tests can reveal the properties of the oxygen vacancies for Mn_2O_3, which is an important factor affecting the catalytic activity.[47] H_2-TPR measurements were performed on the as-prepared pure and Co-/Ni-doped Mn_2O_3 nanowires to reveal their redox properties (Fig. 8). The reduction of Mn_2O_3 sample exhibit

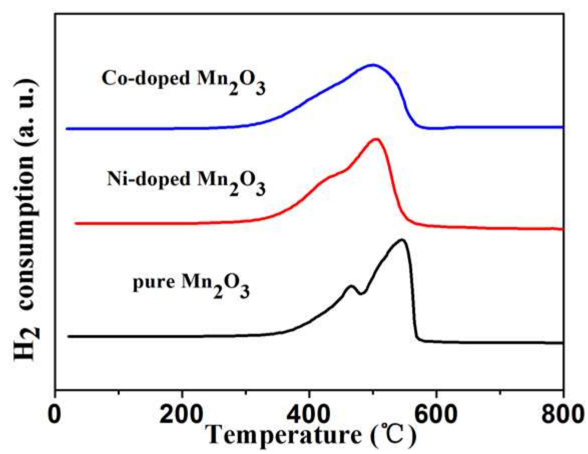

Fig. 8. H_2-TPR profiles of pure Mn_2O_3, Ni-doped Mn_2O_3 and Co-doped Mn_2O_3.

-s two well-defined peaks with the maxima at 469, 541 ^oC. The former (α-peak) is probably attributed to the reduction of Mn_2O_3 to Mn_3O_4 and the higher temperature peak (β-peak) can correspond to the further reduction of Mn_3O_4 to MnO. The reduction of MnO to Mn metal was not detected even up to a reduction temperature of 800 °C, because of its larger negative value of reduction potential.[48] Clearly observed that the reduction peaks firstly shifts to lower temperature, which can be attributed to the reduction of Co^{2+}/Ni^{2+} ion that is incorporated to the crystal lattice of the Mn_2O_3 host. Furthermore, there is a direct proportion relationship between the peak areas of the curves and the amount of H_2 consumption.[49] Here, peak areas of the above three samples (pure, Co^{2+}-, Ni^{2+}-) are with a sequence Co^{2+}- > Ni^{2+}- > pure, which indicates the doped samples have better reducion behavor. All the above confirms the lattice defects and the more surface oxygen species of the doped samples which lead to excellent catalytic properties.

3.3 Catalytic properties

Because of its particular redox property, Mn_2O_3 is an important catalyst. It was discovered that the oxygen in the lattice of Mn_2O_3 surface could react with CO while releasing the oxidation product CO_2 and creating an O vacancy in the lattice.[50] Here, the CO conversion reaction was selected to evaluate the catalytic property of our prepared samples. Fig. 9 displays the catalytic activities of the samples (Ni-doped Mn_2O_3 and Co-doped Mn_2O_3), along with the pure Mn_2O_3 nanowires. No matter pure or doped Mn_2O_3, it can be clearly seen that the catalytic performance of our products have been sharply improved by comparison with commerical Mn_2O_3. As shown in Table1 (supporting) the series of our samples have a large surface area while the commercial ceria are only 5.816 m^2g^{-1}. The BET surface areas data can be a first evidence to explain the difference catalytic property between our products and commercial Mn_2O_3 as a result of the higher surface area can increase more active sites for conversion.[51,52] It was worth mentioning that the rates of the CO conversion of Ni-doped and Co-doped Mn_2O_3 nanowires were considerably fast with a temperature scale of about 80 °C and75 °C, respectivly.

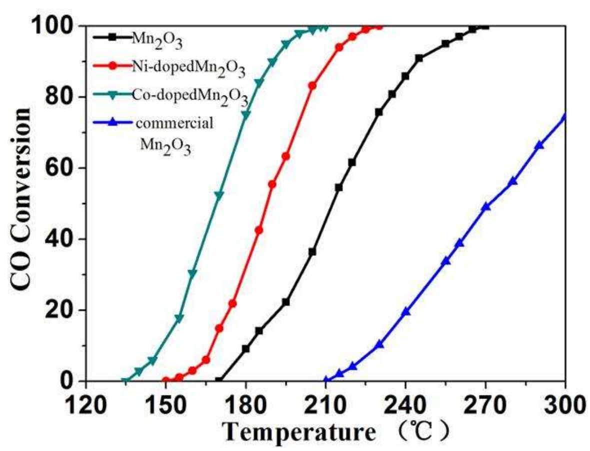

Fig.9 Percentage conversion versus temperature plots for the oxidation of CO over Mn_2O_3, Ni-doped Mn_2O_3 and Co-doped Mn_2O_3.

But, the evaluated temperature of the pure Mn_2O_3 nanowires is from 170 °C to 270 °C. The increased catalytic activity of the doped products is due to the increased surface area and the promoted active oxygen content caused by ions' substitution. Luo et al. has reported the oxidizing of CO on the α-Mn_2O_3 surfaces may proceed through the Langmuir-Hinshelwood mechanism (<220°C) to Mars-van-Krevelen mechanism (>350°C) with the increasing of reaction temperature.[32] In fact, all of our Mn_2O_3 nanowire materials oxidize CO by a Langmuir-Hinshelwood mechanism, in which the role of the dopant is to facilitate the formation of oxygen vacancies. The CO oxidization process can be divided into three stages, the O_2 dissociative adsorption [Equations (1) and (2)] and its surface reaction with CO [Equation (3)] [53]

$$O_{2(g)} + \oplus \rightarrow O_2\text{-}\oplus \quad (1)$$
$$O_2\text{-}\oplus + \oplus \rightarrow 2O\text{-}\oplus \quad (2)$$
$$CO\text{-}* + O\text{-}\oplus \rightarrow CO_{2(g)} + * + \oplus \quad (3)$$

*and ⊕ denote metal and support sites, respectively.

In the case of Mn_2O_3, a surface phase transformation from α-Mn_2O_3 to MnO-like species, during the adsorption and oxidation of CO for the first time. An oxygen vacancy is created in the process. The oxygen gas then reacts with the surface to regenerate a surface oxygen atom [Equation (1), (2)]. Highly reactive atomic oxygen is formed due to the dissociation of molecular oxygen at the vacancy site.[26] Finally, CO reacts with the highly active atomic oxygen to generate CO_2[Equation (3)]. When Ni^{2+}, Co^{2+} cations were incorporated into Mn_2O_3 lattice, the extra oxygen vacancies were generated to compensate for the valence mismatch between Ni^{2+}/Co^{2+} and Mn^{3+}. A large amount of oxygen vacancies not only promote the dissociation of reactants by strong binding, but also produce excess electrons[54,55], which tend to localize on the near pair of Mn^{3+} due to unreducible Co^{2+} and Ni^{2+} doped into the lattice, and result in highly reducible Mn_2O_3. More than that, the smaller Ni and Co dopants can set some space free to accommodate the bigger Mn^{2+}, which helps to release the lattice strain and to get the lattice energy down.[56] Therefore, the enhanced catalytic activity of Ni^{2+}-/ Co^{2+}-doped Mn_2O_3 can be attributed to the lattice change and the promoted oxygen vacancies, which can increase catalytically active sites. Notably, it's worth considering the higher catalytic performance Co-doped Mn_2O_3 nanaowires have than Ni-doped Mn_2O_3 was due to the actual doping amount and the intrinsic characteristics of cobalts and nickel on the catalytic activity. In fact, the essential distinction is under investigation, which will be presented in our future work.

To demonstrate the thermal stability of the as-prepared Mn_2O_3 nanowires, the recycling catalytic tests were performed 6 times. It was found that the catalytic efficiency remains nearly constant for Co-doped (Fig. 10a), and Ni-doped (Fig. 10b) along with pure (Fig. S3) Mn_2O_3, which can be demonstrating its excellent stability and recycling performance. Expectedly, the features of the catalysts remain almost unchanged after the 6 times' catalysis, which are confirmed by the SEM images (Fig. S1) and XRD patterns (Fig. S2) (Supporting). It is obvious that our as-prepared cation-doped Mn_2O_3 nanowires catalysts possess a desirable stability.

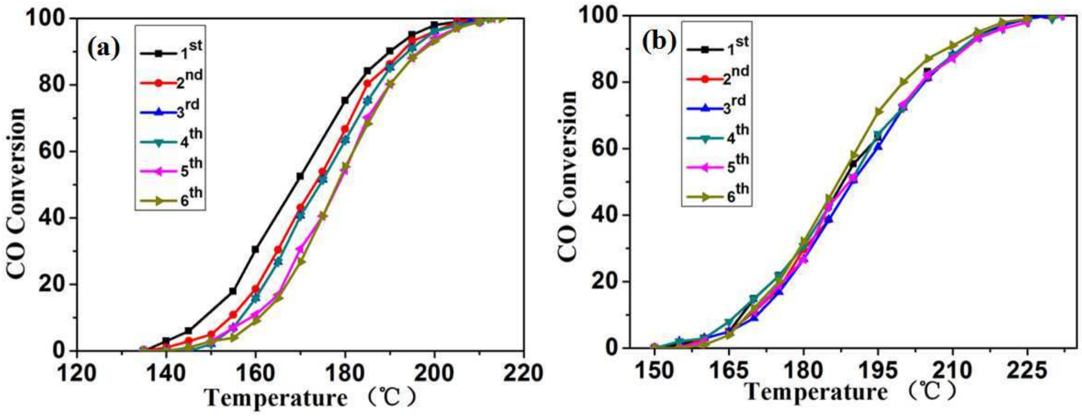

Fig. 10 Catalytic performance of Co-doped Mn_2O_3 (a) and Ni-doped Mn_2O_3 (b) in different runs.

4 Conclusions

In summary, we have obtained Ni-doped and Co-doped manganese oxides (Mn_2O_3) 1 D nanowire via a solvothermal synthesis followed by calcination that free of template-assisted route, and the composition and morphology can be easily controlled by the use of different dopants as reactants. Preliminary catalytic results indicated that Ni-, Co-doped Mn_2O_3 had excellent catalytic activity towards CO oxidation. With the help of SEM, XRD, Raman, EDS mapping and HRTEM, XPS, H_2-TPR, we achieved a better understanding of the phenomena that Ni^{2+}, Co^{2+} incorporated into the Mn_2O_3 lattice leading to richer oxygen vacancies, which contributed to the improvement of the catalytic performance in CO oxidation of our doped samples.

5 Acknowledgements

This work was supported by the Natural Science Foundation of China (grant no. 21276142 and 21476129).

Supporting Information

The surface areas and the compositional data of the as prepared Mn_2O_3 samples. SEM and XRD of Ni-doped Mn_2O_3 and Co-doped Mn_2O_3 nanowires after catalysis for 6 times. Catalytic performance of pure Mn_2O_3 nanowires in different runs.

References

1 B. H. Liang, S. Liu, and S. Yu, *Adv. Mater.*, 2010, **22**, 3925-3937.
2 B. H. Park, S. Lee, T. W. Kim, S. T. Lim, S. Hwang, Y. Yoon, Y. Lee, and J. Choy, *Adv. Funct. Mater.*, 2007, **17**, 2949-2956.
Q. Javed, F. P. Wang, M. Y. Rafique, A. M. Toufiq, Q. S. Li, H. Mahmood and W. Khan, *Nanotechnology.*, 2012, **23**,415603.
3 Y. Guo, L. Xu, H. Liu, Y. Li , C. Che, and Y. Li, *Adv. Mater.*, 2015, **27**, 985-1013.
4 R. S. Devan, R. A. Patil, J. Lin, and Y. Ma., *Adv. Funct. Mater.*, 2012, **22**, 3326-3370.
5 Y. L. Wang, X. C. Jiang, and Y. N. Xia , *J. Am. Chem. Soc.*, 2003, **125**, 16176-16177.
6 G. X. Wang, J. S. Park, M. S. Park, and X. L. Gou, *Sens. Actuators B.,* 2008, **131**, 313-317.
7 V. T. Le, T. N. L. Le , and V. H. Nguyen, *Sens. Actuators B.,* 2010, **150**, 112-119.
8 Z. Zeng, P. Sun, J. Zhu, and X. Zhu, *RSC Adv.*, 2015, **5**. 17550-17558.
9 Y. B. He, G. R. Li, Z. L. Wang, C. Y. Su, and Y. X. Tong, *Energy Environ. Sci.*, 2011, **4**, 1288-1292.
10 C. Pan, D. Zhang, L. Shi, and J. Fang. *Eur. J. Inorg. Chem.*, 2008, **10**, 2429-2436.
11 C. Pan, D. Zhang, and L. Shi, *Journal of Solid State Chemistry.*, 2008, **181**, 1298-1306
12 S. Liang, F. Teng, G. Bulgan, R. Zong, and Y. Zhu. *J. Phys. Chem. C.*, 2008, **112**, 5307-5315.
13 V. B. R. Boppana and F. Jiao, *Chem. Commun.*, 2011, **47**, 8973-8975.
14 W. Zheng, Y. F. Zheng, K. W. Jin, and N. Wang, *Talanta.*, 2008, **74**, 1414-1419.
15 M. A. Kumar, S. Jung, and T. Ji , *Sensors.*, 2011, **11**, 5087-5111.
16 S. Carrettin, P. Concepcion, A. Corma, J. M. L. Nieto and V. F. Puntes, *Angew. Chem., Int. Ed.*, 2004, **43**, 2538-2540.
17 H. X. Mai, L. D. Sun, Y. W. Zhang, R. Si, W. Feng, H. P. Zhang, H. C. Liu and C. H. Yan, *J. Phys. Chem. B.*, 2005, **109**, 24380-24385.
18 M. Nolan, S. C. Parker and G. W. Watson, *Surf. Sci.*, 2005, **595**, 223-232.
19 C. Zhang, L. Han, W. Liu, H. Yang, X. Zhang, X. Liu and Y. Z. Yang, *CrystEngComm.*, 2013, **15**, 5150-5155.
20 B. Ammundsen, and J. Paulsen, *Adv. Mater.*, 2001, **13**, 943-956.
21 S. J. Hwang, H. S. Park, J. H. Choy, and G. Campet, *J. Phys. Chem. B.,* 2000, **104**, 7612-7618.
22 D. Hong, Y. Yamada, A. Nomura, and S. Fukuzumi, *Phys. Chem. Chem. Phys.*, 2013, **15**, 19125-19128.
23 M. M. Najafpour, T. Ehrenberg, M. Wiechen and P. Kurz, *Angew. Chem., Int. Ed.*, 2010, **49**, 2233-2237.
24 M. M. Najafpour, B. Pashaei and S. Nayeri, *Dalton Trans.*, 2012, **41**, 4799-4805.
25 T. Y. Li, G. L. Xiang, J. Zhuang and X. Wang, *Chem. Commun.*, 2011, **47**, 6060-6062.
26 F. Yang, J. Wei, W. Liu, J. Guo, and Y. Yang. *J. Mater. Chem. A.*, 2014, **2**, 5662-5667.
27 X. Niu, H. Wei, W. Liu, S. Wang, J. Zhang and Y. Yang. *RSC Adv.*, 2015, **5**, 33615-33622.
28 H. Zhou, Y. Shi, Q. Dong, J. Lin, A. Wang, and T. Ma, *J. Phys. Chem. C.*, 2014, **118**, 20100-20106.
29 Y. Yin and A. P. Alivisatos, *Nature.*, 2005, **437**, 664-670.
30 D. Chen and Y. Wang. *Nanoscale.*, 2013, **5**, 4621-4637.
31 Y. Dai, H. Jiang, Y. Hu and C. Li, *RSC Adv.*, 2013, **3**, 19778-19781.
32 Y. Luo, Y. Deng, W. Mao, X. Yang, K. Zhu, J. Xu, and Y. Han, *J. Phys. Chem. C.*, 2012, **116**, 20975-20981.
33 Y. Han, K. Ramesh, L. Chen, E. Widjaja, S. Chilukoti, and F. Chen. *J. Phys. Chem. C.*, 2007, **111**, 2830-2833.
34 J. Zhang, G. Cai, D. Zhou, H. Tang, X. Wang, C. Gu and J. Tu, *J. Mater. Chem. C.*,2014, **2**,7013-7021.
35 M. A. Vuurman, D. J. Stufkens, A. Oskam, G. Deo and I. E. Wachs, *J. Chem. SOC., Faraday Trans.*, 1996, **92**, 3259-3265.
36 F. Arena, G. Trunfio, J. Negro, B. Fazio, and L. Spadaro, *Chem. Mater.*, 2007, **19**, 2269-2276.
37 W. Liu, X. F. Liu, L. J. Feng, J. X. Guo, A. R. Xie, S. P. Wang, J. C. Zhang and Y. Z. Yang, *Nanoscale.*, 2014, **6**, 10693-10700.

38 Y. Lee, G. H. He, A. J. Akey, R. Si, M. Flytzani-Stephanopoulos, and I. P. Herman, *J. Am. Chem. Soc*. 2011, **133**, 12952-12955.
39 G. Avgouropoulos, T. Ioannides, H. K. Matralis, J. Batista and S. Hocevar, *Catal. Lett*., 2001, **73**, 33-40.
40 L. Zhao, X. Li, J. Zhao, *Applied Surface Science*., 2013, **268**, 274-277.
41 L. Fu, Z. Liu, Y. Liu, B. Han, P. Hu, L. Cao and D. Zhu, *Adv. Mater*., 2005, **17**, 217-221.
42 B. Ernst, S. Libs, P. Chaumette and A. Kiennemann, *Appl. Cata*l. A., 1999, **186**, 145-168.
43 D. Hong, Y. Yamada, T. Nagatomi, Y. Takai, and S. Fukuzumi. *J. Am. Chem. Soc*., 2012, **134**, 19572-19575.
44 M. M. Rahman, S. B. Khan, M. Faisal, M. A. Rub, A. O. Al-Youbi, and A. M. Asiri. *Talanta*., 2012, **99**, 924-931.
45 X. Y. Zhang, J. J. Wei, H. X. Yang, X. F. Liu, W. Liu, C. Zhang, and Y. Yang, *Eur. J. Inorg. Chem*., 2013, **25**, 4443-4449.
46 S.P. Wang, X. C. Zheng, X. Y. Wang, S. R.Wang, S. M. Zhang, L. H. Yu, W. P. Huang, and S. H. Wu, *Catal. Lett.,* 2005, **105**, 163-168.
47 J. Ke, J. W. Xiao,W. Zhu, H. C. Liu, R. Si, Y. W. Zhang and C. H. Yan, *J. Am. Chem. Soc.*, 2013, **135**, 15191-15200.
48 M. Luo, X. Yuan, X. Zheng. *Applied Catalysis A*., 1998, **175**, 121-129.
49 J. Zhang, H. Yang, S. Wang, W. Liu, X. Liu, J. Guo and Y.Yang, *CrystEngComm.*, 2014, **16**, 8777-8785.
50 D. K. Kim, K. Stöwe, F. Müller, and W. F. Maier, *J. Catal*., 2007, **247**, 101-111.
51 C. M. A. Parlett, Karen Wilson and A. F. Lee, *Chem. Soc. Rev.*, 2013, **42**, 3876-3893.
52 S. Y. Lai, Y. Qiu and S. Wang, *J. Catal*., 2006, **237**, 303-313.
53 S. Royer and D. Duprez, *ChemCatChem*., 2011, **3**, 24-65.
54 M. Nolan, S. C. Parker and G. W. Watson, *J. Phys. Chem. B*., 2006, **110**, 2256-2262.
55 M. Nolan, S. C. Parker and G. W. Watson, *Surf. Sci*., 2006, **600**, 175-178.
56 Z. Yang, Z. Fu, Y. Wei and Z. Lu, *J. Phys. Chem. C*., 2008, **112**, 15341-15347.